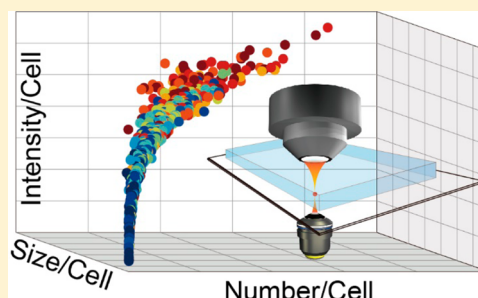


Label-Free Digital Quantification of Lipid Droplets in Single Cells by Stimulated Raman Microscopy on a Microfluidic Platform

Chen Cao,[†] Dong Zhou,^{†,‡} Tao Chen,^{†,‡} Aaron M. Streets,^{*,†,‡,§} and Yanyi Huang^{*,†,‡,¶}[†]Biodynamic Optical Imaging Center (BIOPIC), School of Life Sciences, Peking University, Beijing 100871, China[‡]College of Engineering, Peking University, Beijing 100871, China[¶]Peking-Tsinghua Center for Life Sciences, Peking University, Beijing 100871, China

Supporting Information

ABSTRACT: Quantitative characterization of a single-cell phenotype remains challenging. We combined a scalable microfluidic array of parallel cell culture chambers and stimulated Raman scattering (SRS) microscopy to quantitatively characterize the response of lipid droplet (LD) formation to free-fatty-acid stimuli with single-LD resolution at the single-cell level. By enabling the systematic live-cell imaging with SRS microscopy in a microfluidic device, we were able to quantify the morphology of over a thousand live cells in 10 different chemical environments and with 8 replicates for each culture condition, in a single experiment, and without relying on fluorescent labeling. We developed an image processing pipeline for cell segmentation and LD morphology quantification using dual-channel SRS images. This allows us to construct distributions of the morphological parameters of LDs in the cellular population and expose the vast phenotypic heterogeneity among genetically similar cells. Specifically, this approach provides an analytical tool for quantitatively investigating LD morphology in live cells in situ. With this high-throughput, high-resolution, and label-free method, we found that LD growth dynamics showed considerable cell to cell variation. Lipid accumulation in nonadipocyte cells is mainly reflected in the increase of LD number, as opposed to an increase in their size or lipid concentration. Our method allows statistical single-cell quantification of the LD distribution for further investigation of lipid metabolism and dynamic behavior, and also extends the possibility to couple with other “omics” technologies in the future.



Quantifying cellular behavior is an important way to provide in-depth insights into metabolism and can lead to advances in medicine. Until recently, the majority of biological measurements have been performed on bulk samples to provide information about averaged populations, while obscuring the state of small subpopulations or outlier cells. However, cellular heterogeneity is a fundamental feature of many biological processes, and the characterization of cell-to-cell variation by several emerging imaging technologies has been proved to help the deconvolution of mixed cell populations.^{1–3}

The metabolic pathway is a system which exhibits significant intercellular variability. As one of the most conserved pathways in metabolism, lipid metabolism has drawn great interest because of its strong association with obesity, diabetes, and other metabolic syndromes.⁴ It is critical to investigate the emergence and the consequence of heterogeneity in such a complex biosystem. Microscopic imaging has always been suitable to interrogate single cells in detail, offering a massive amount of data of cell morphology and assessing the difference between cells. For example, single-cell size analysis of the subcutaneous adipocytes explained the relationship between fatty acid uptake and insulin sensitivity by employing a new imaging assay.⁵ The significance of such kind of single-cell studies highlights the need of high-throughput, systematic

approaches to collect quantitative information about the phenotypic and genotypic characteristics of single cells. Thus, technologies for investigating the heterogeneity of response in single cells are of great interest.

Lipid droplets (LDs), known as an energy reservoir organelle in almost all types of eukaryotic cells, are crucial for lipid metabolism. The phenotypic heterogeneity of LDs is now appreciated as an important component in physiology and metabolism.⁶ The features of LDs vary across different cell types, and even differs considerably between individual cells of populations.^{4,7,8} Previous studies based on large populations of cells mostly reported averaged measurements of LD phenotype without distinguishing the intrinsic LDs distribution among cells. The phenotypic heterogeneity of LDs is now appreciated to be associated with both the intrinsic gene regulation and external chemical stimuli,^{9,10} and recent research even suggests that the cell variability in LD morphology indicates a mechanism to reduce lipotoxicity.³ In addition, the discovery of the influence of adipokines on physiology and metabolism^{6,11} implies that the heterogeneity in adipogenesis may interfere with the efficacy of drugs aiming at adipocyte

Received: March 4, 2016

Accepted: April 4, 2016

Published: April 4, 2016

differentiation. Tracing the origin of such variability in lipid metabolism will not only open a door to many new biological questions but also improve the treatment of lipid metabolism diseases and the drug efficiency evaluation. The need of LD quantification with single-cell resolution is therefore necessary and acute.

Statistical analysis of cell-to-cell heterogeneity in LD characteristics requires the collection of data from a large number of cells under varying conditions in a systematic fashion. However, experiments using manual pipetting and dish-based cell culture methods have limited the throughput and reproducibility. Microfluidic technology^{12,13} largely overcomes these difficulties by precise fluidic control, automated manipulation of chemical delivery, multiplexing potential, and low reagent consumption. Combined with fluorescent live-cell microscopy, microfluidics-based cell culture platforms have contributed to a better understanding of stem cell differentiation,¹⁴ cell migration,¹⁵ signaling dynamics,^{16,17} and other processes.^{18–20} However, for LD quantification, fluorescent labeling is not always an optimal solution. In some cases, the intercalation of fluorescent molecules can alter the properties of lipid-rich structures,^{21,22} and the labeling efficiency of fluorescent lipid molecules in different cells also poses a problem to the quantitation of LDs.²³ Furthermore, nonspecific binding and diffuse staining of fluorescent dyes may lead to misleading conclusions from image analysis.^{24,25} As an alternative to fluorescence, nonlinear optical imaging, which probes the intrinsic optical properties of molecular structures, provides an attractive approach for quantifying LDs. In particular, stimulated Raman scattering (SRS) microscopy²⁶ has been used in the study of lipid biology in recent years.^{27–30} In SRS, when the beating frequency of pump and Stokes beams matches the C–H bond stretching frequency of CH₂ groups, a strong signal is produced from lipid rich structures. In this way, long-term three-dimensional live cell imaging with SRS is not limited by photobleaching. Additionally, the intensity of SRS signal is proportional to the number of chemical bonds in the detection foci,²⁶ which makes the quantification of LDs straightforward to carry out. The combination of microfluidic technology and SRS microscopy presents an ideal approach to performing quantitative studies on lipid metabolism with single-cell resolution.

Here we developed a scalable microfluidic array of parallel cell culture chambers capable of titrating reagents into the extracellular environment of independently addressable nanoliter cell culture colonies. We also constructed a SRS microscope that is capable of acquiring a Raman signal, propagating through the microfluidic device, from the cells cultured on-chip. With this integrated system, we performed a systematic imaging of cell colonies exposed to varying amounts of extracellular fatty acid. We also developed an automated image processing algorithm suitable for multichannel chemical images, with which the number, volume, and intensity of single LDs were quantified at the single-cell level. We applied this integrated platform to the study of the free fatty acid uptake process, which stimulates the formation of LDs in nonadipocyte cells, and we demonstrated the dominant accumulation mechanism of LDs in multiple types of cells based on statistical analysis of single LDs and single cells. This high-throughput approach provided a quantitative landscape presenting the cell to cell variation of LD growth dynamics.

■ EXPERIMENTAL SECTION

Cell Culture on Chip and Device Operation. The channels of the microfluidic device include the cell flow channels and reagent flow channels (see Figure S1 in the Supporting Information). Before use, all of the valves were injected with sterilized water and pressurized with 30 psi. All of the flow channels were washed with sterilized water and air-dried. The cell flow channels were then incubated with 10 mg/mL fibronectin (F0895, Sigma-Aldrich, U.S.A.) at 37 °C for 60 min. After incubation, the cell flow channels were rinsed with sterilized water thoroughly, air-dried, and filled with fresh culture medium. All of the valves were closed before seeding cells. After the valves controlling the waste channel and the Cell/Medium Outputs were opened, the cell suspension was injected onto the chip from the Cell/Medium Input by sterilized gel-loading tips (2239916, Bio-Rad Laboratories, U.S.A.), which were pressurized with 5 psi. When a steady and uniform flow of cells was introduced, the waste channel valve was closed, and the valves controlling cell culture chambers (containment valves in Figure S1) were opened one at a time to let the cells flow through. After every chamber in a column was filled with cells (typically ~15–20 cells/chamber), the containment valve of this column was closed. This procedure was repeated for all of the eight columns. For experiments in which multiple cell types were cultured on the same chip, after one cell type was successfully seeded on the chip, the Cell/Medium Input and the waste channel were thoroughly flushed with sterilized water until all of the cells were washed away and air-dried to prevent cross contamination between different kinds of cells. Then the waste channel was filled with fresh medium again; subsequently, a different cell type could be injected onto the chip, and the cell seeding procedures were repeated.

After cells were attached (~2 h), the microfluidic device with cells was incubated overnight at 37 °C in a humidified incubator with 5% (v/v) CO₂ to attain a stable cell state. The culture medium was automatically changed every 2 h through a LabVIEW (National Instruments) program. Cells can live and divide healthily on chip for at least 3 days (see Figure S2 in the Supporting Information). We seeded HeLa cells on chip and in common dishes, and we compared the cell morphology and the average LD intensity in different concentrations of oleic acid separately (see Figure S3 in the Supporting Information). The comparable results indicate that the microfluidic system provides a cell culturing environment as stable as in Petri dishes. During medium change, a sterilized gel-loading tip with cell culture medium was injected into the cell/medium input and pressurized with ~1–2 psi. The medium change time for each column was 5 min. Then the oleic acid was injected onto the chip from the OA Input by sterilized gel-loading tips, which were pressurized with 5 psi. After the oleic acid channels were fully filled, the pressure of mixing valves were adjusted down to 10 psi (other valves were pressurized by 30 psi), and all of containment valves were kept closed in order to preserve the oleic acid titration. Then the interface valves (see Figure S1 in the Supporting Information) were opened, and the mixing valves were actuated for 30 min at 1 Hz. During the mixing step, the chip with cells was put in the CO₂ incubator. The final concentration of oleic acid was determined by the input oleic acid concentration, and the volume ratio between the cell culture chamber and the oleic acid chamber (see Figure S1 in

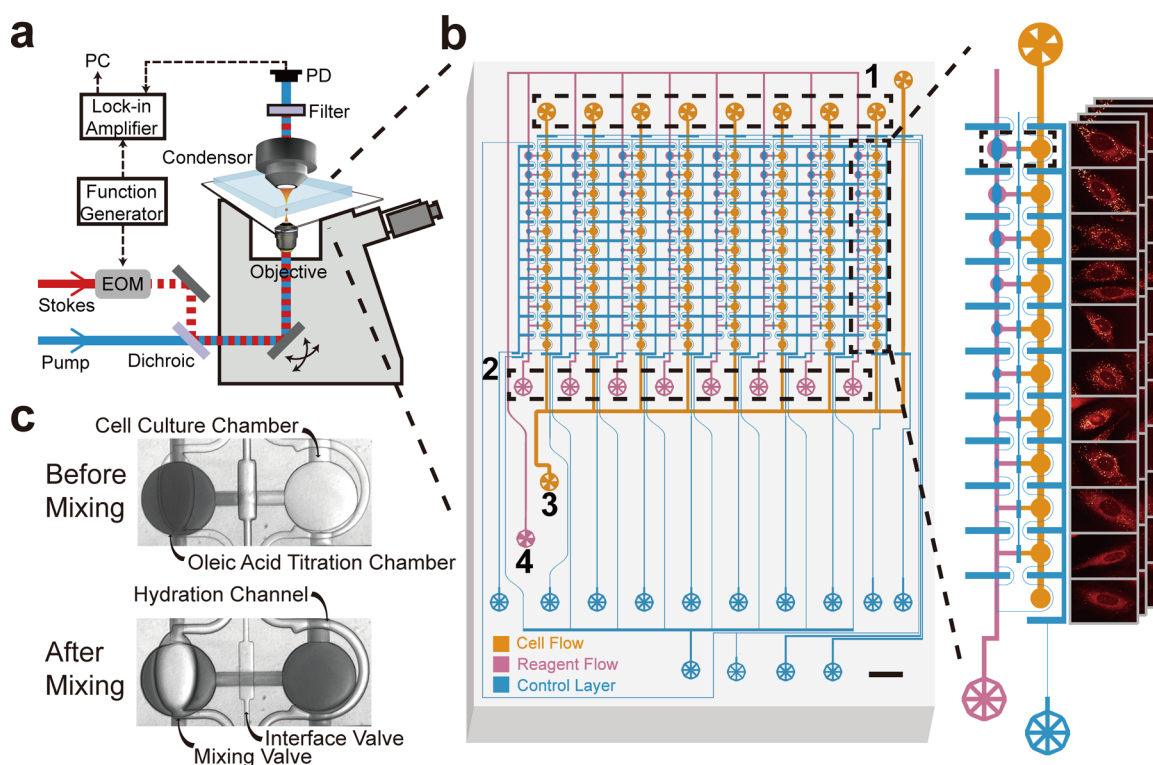


Figure 1. System schematic diagram and the experimental workflow. (a) Setup of the SRS microscope. The microfluidic cell culture chip and SRS imaging platform were combined to quantify lipid droplets morphology change in situ. Pump beam and Stokes beam, modulated by an electro-optical modulator (EOM), were collimated and directed into a scanning microscope and then focused onto the sample. Transmitted light was collected by a long-working distance condenser to allow the use of microfluidic devices and transformed to an electronic signal by a photodiode (PD) after filtering out the Stokes beam. Then the signal was sent into lock-in amplifier and demodulated for image reconstruction in computer. (b) The design of the microfluidic chip (scale bar: 2 mm). Orange and pink lines represent the flow channels, and blue lines are the control channels. Numbers 1–4 label regions of the cell/medium output, OA output, cell/medium input, and OA input, respectively. The different volume ratio between the cell culture chamber (orange) and the OA chamber (pink) generates various concentrations of OA. Cell colonies in each cell culture chamber were imaged under SRS microscopy. (c) Micrographs of one pair of cell culture chamber and OA chamber before (top) and after (bottom) mixing. Here colored dye was injected into OA chamber, and clean water was injected into the cell culture chamber for mixing demonstration. The calculation of mixing efficiency and other details are explained in the [Experimental Section](#).

the [Supporting Information](#)). Cells were incubated with oleic acid concentration for 3 h before imaging.

Image Processing. We used 512×512 images in our study, as the lipid droplet (LD) is a highly dynamic organelle, and its measurement asks for a balance between the time resolution and spatial resolution, especially when 3-D live-cell imaging is applied (see Figure S4 in the [Supporting Information](#)). We developed our imaging processing algorithm for LD quantification of SRS images. The custom scripts were written in MATLAB. Compared with LDs in mature adipocytes, the size of LDs in nonadipocytes cells is much smaller,^{4,7} yielding a relative low contrast between LDs and the cytoplasm. Additionally, other cell organelles with membrane-rich structures, like ER, may also be probed by SRS in lipid band and generate irregular background pattern (see Figure S5–6 in the [Supporting Information](#)). Thus, background removal is crucial in SRS images processing. Under low excitation power, the lipid content in these organelles was very low and widely distributed, and thus, their contribution to SRS signals was much less compared with that of lipid droplets. For both the lipid-specific images (CH_2 stretching vibration, 2850 cm^{-1}) and protein-specific images (CH_3 stretching vibration, 2950 cm^{-1}), the first step was to perform background smoothing to each slice of the image stack by morphology top-hat filtering. For lipid-specific images, an intensity threshold

was set for eliminating small residues with low intensity noise which might come from the fine fluctuation of morphology top-hat filtering. The remaining signals were binarized to generate a LD mask. As the 3-D images are cubic arrays in space, with a field of view of $211 \times 211 \mu\text{m}^2$, one single pixel in a 512×512 image represents about half a micron. We considered that, first, LDs are approximately spherical, and second, LDs less than one micron are barely detected because of the diffraction limit. Hence, eight pixels representing about one cubic micron were taken as a conservative filter, and any connected objects in three dimensions that had fewer than eight pixels were removed from the binary mask. The processed LD mask was then used for calculating total LD size and intensity by counting the number of pixels per droplet and then mapping each pixel's intensity back to the mask area and summing them across the image stack.

In the lipid-specific channel, the scattered spatial distribution of the lipid-rich structures in the cell makes automated cell boundary segmentation challenging in SRS images. While for protein, because of the existence of cytoskeleton, protein distribution in cells are more abundant and uniform, resulting in a high contrast between the cell and the background in protein-specific images. Therefore, protein-specific images efficiently reveal information about the cell outlines. For protein-specific images, after background removal, Otsu's

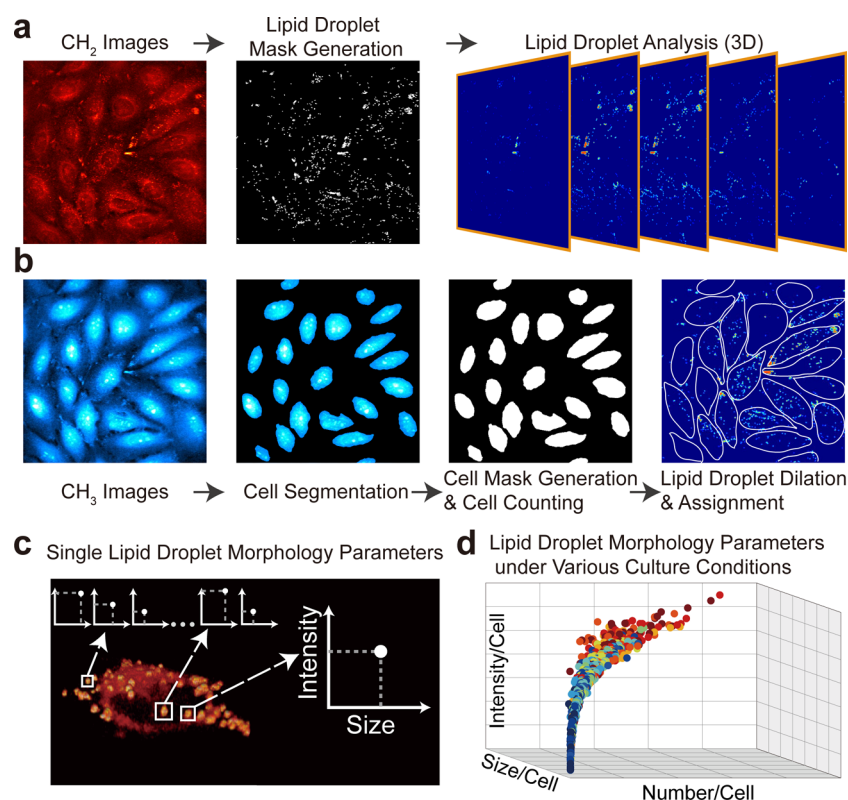


Figure 2. SRS images processing. (a) The schematic of major steps of lipid-specific images processing. 3-D lipid-specific images were acquired at 2850 cm^{-1} (CH_2 stretching vibration) and went through LD mask generation, signal filtering, LD connectivity recognition and quantification (Experimental Section). (b) The schematic of major steps of protein-specific images processing. 3-D protein-specific images were acquired at 2950 cm^{-1} (CH_3 stretching vibration) and went through cell boundary segmentation, cell mask generation, LD dilation and assignment. Automated LD quantification at single-cell level requires the information on both CH_2 and CH_3 images. Other details about image processing are explained in the Experimental Section. (c) For each LD, the intensity and size can be measured by our platform. (d) For each cell cultured in different concentrations of OA, the total size, intensity, and number of LD can be quantified. The relationship of these LD morphology parameters among single cells can be inferred under various culture conditions (a dot-plot shows a possible relation among those parameters, and different colors of dots represent different culture conditions).

method³¹ was used for computing the global threshold followed by multidimensional filtering to generate a binary cell mask. In some instances, cells were so confluent that their boundaries were connected to each other. In these instances, congregated cells may be mistaken for single cells, and the algorithm will thus underestimate the cell number. Thus, it is very important to control the cell density for accurate cell segmentation. Then the LDs imaged in the same field of view were assigned to each cell area according to their coordinates with respect to the cell mask. As the edges of cultured adherent cells commonly spread out, making the efficient concentration of peripheral protein relatively low in focus, the binarized cell mask areas were often smaller than the original cells. In order to map the undetermined peripheral LDs to their proper cells of origin, we adopted an algorithm of dilation which expanded the area of LDs in succession until they were in the closest cell's mask to which they were assigned.

RESULTS AND DISCUSSION

High-Throughput Cell Culture and Microenvironment Control on Microfluidic Chip. We used double-layer soft lithography to build a polydimethylsiloxane (PDMS) microfluidic device featuring 88 addressable cell culture chambers (Figure 1 and Figure S1). This scalable microfluidic device was composed of eight units. Each unit was independently operated by integrated microvalves, making multiple types of cell culture

on the same chip accessible. In each unit, 11 cell culture chambers were arrayed in a row, parallel with a titration row possessing ten chemical storage chambers with variable volumes and one “negative control” chamber (Figure 1b and Figure S1). This design provides comprehensive observation of the dynamics of cellular response to chemical stimulus, in our case the free fatty acid (FFA). Each cell culture chamber harbored a volume of 5.9 nL, which is about a million-fold decrease from traditional 30 mm cell culture dish. The permeability of PDMS not only ensures the sufficient exchange of oxygen and carbon dioxide but also causes the dehydration as the water evaporates through it. To circumvent this problem, we added a hydration channel which encompassed the cell culture chamber to help increase the moisture supply (Figure 1c and Figure S1b). Interface microvalves were designed to control the communication between each pair of cell culture chamber and the oleic acid chamber (Figure 1b and Figure S1b). After oleic acid was injected into the titration array, the interface microvalves were opened, and the mixing valves were actuated. The mixing efficiency was measured by optical absorption (see Figure S7 in the Supporting Information), and no disturbance of cells was observed during mixing. The microfluidic device with cell colonies was then imaged for each chamber under SRS microscopy, followed by quantitative image analysis.

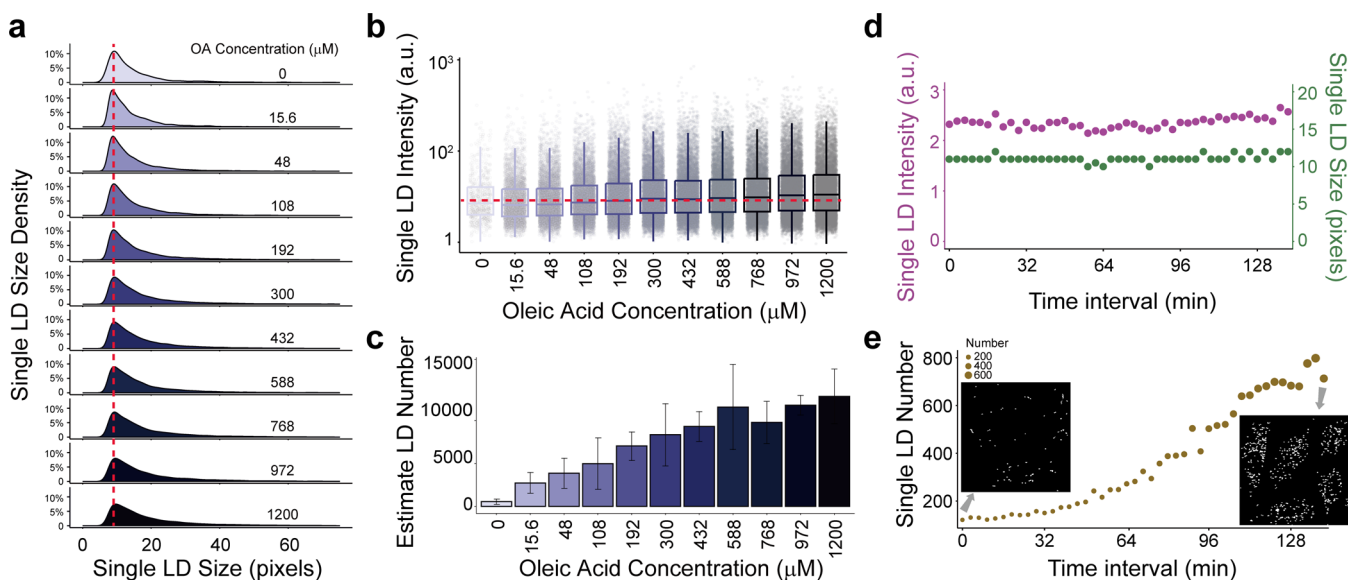


Figure 3. Single lipid droplet distribution in HeLa cells. Single LD was filtered by the size and the circularity of the LD (Experimental Section). (a) The density plot of single-LD size of HeLa cells cultured with the OA concentration ranging from 0 to 1.2 mM. (b) Single LD intensity distribution of HeLa cells cultured from low to high concentrations of OA. Each dot denotes the intensity of a single LD. (c) The estimated LD number in HeLa cells cultured with different concentrations of OA. (d,e) LD quantification in time lapse imaging of cells in one chamber of the chip. (d) The single-LD size and intensity distribution. (e) The estimated number of LDs. The cropped LD masks from the beginning and the end of the time lapse video are shown.

Lipid Droplet Quantification through SRS Imaging.

Stimulated Raman scattering (SRS) microscopy offers high-resolution three-dimensional label-free imaging of live cells with chemical specificity.^{26,29,30} Moreover, the intensity of the SRS signal is proportional to the number of specific chemical bonds in the detection foci,²⁶ making the substance quantification straightforward. One unique and critical instrumental component in our SRS microscope is a long-working-distance condenser, which allows optical signal collection through the thick PDMS microfluidic device. Using dual-band label-free Raman images obtained at 2850 and 2950 cm^{-1} , representing the spatial distribution of CH_2 and CH_3 groups, respectively, we developed an automated image processing pipeline using a linear combination of the intensity of both bands to quantitatively characterize the number, size, and signal intensity of intracellular LDs in single cells under various concentrations of exogenous oleic acid (OA) with single-LD resolution and at the single-cell level.

We first corrected unevenly distributed background of each slice in the image stack by morphology top-hat filtering (see Figure S5–6 in the Supporting Information). The remaining signal was binarized to generate a lipid droplet mask (Figure 2a). To ensure the authenticity of LD signals, we further constrained the size of objects in the mask (Figure 2a). The processed lipid droplets mask was then used for calculating total LDs' size and intensity by mapping each pixel's signal back to the mask area and summing them up across the image stack.

To quantitatively assess the heterogeneity of LD distribution of single cells, we obtained both images at 2850 and 2950 cm^{-1} in the same field of view in our system (Figure 2a,b). We used CH_3 -channel images to extract the boundaries of each single cell and then generated a cell mask for further analyses (Figure 2b). The cells were segregated, counted, and indexed with CH_3 -channel images, and then, using the CH_2 -channel images, the position of each LD was recorded and assigned to the cell (Figure 2b). For those undetermined LDs, we adopted the

algorithm of dilation which expanded the area of LDs in succession until they located in the range of a cell's mask (Figure 2b).

With this image-processing algorithm, the morphology parameters of every LD, including the position, number, volume, and intensity, were quantified (Figure 2c). In addition, LD heterogeneity between single cells can be accessed under various microenvironment conditions (Figure 2d). As the long-term three-dimensional live cell imaging with SRS is not limited by photobleaching, we were capable of recording and quantifying the dynamic change of LDs (see Video S2 in the Supporting Information). Thus, digital quantification of LDs by SRS microscopy capacitates abundant information acquisition in a high throughput fashion.

Single Lipid Droplet Distribution in HeLa. We first applied this integrated culture-imaging system to investigate LD growth dynamics in HeLa cells. In theory, the OA induced lipid accumulation will be reflected in the LD formation and growth by increasing the number, the average size, or the average intensity of LDs, or a combination of these mechanisms. The interplay between these LD growth mechanisms reveals different aspects of the biochemical lipid regulation.⁸ Identification of the dominant mechanism therefore may help to inform the theoretical model of LD formation and improve our understanding of energy utilization. Thus, statistical and quantitative investigation of the morphological change of LDs during growth is of great importance.

We examined 11 different HeLa culture conditions with the OA concentration ranging from 0 to 1.2 mM (Figure 3a–c). The experiment had three replicates, yielding imaging data of 3466 live cells. In total, 98 932 single LDs (see Figure S8 in the Supporting Information) were identified by label-free SRS microscopy for further quantitative analyses. The size of single LDs was consistent when cells were exposed to different concentrations of OA (P value = 0.8923, Figure 3a). Similarly, the intensity of single LDs (i.e., the total amount of lipid inside

each LD) between various conditions did not show significant variation (P value = 0.8777, Figure 3b). However, compared to the OA-free culture condition, the number of LDs in HeLa cells increased significantly by about a factor of 10 when exposed to 1.2 mM OA (P value = 4.673×10^{-14} , Figure 3c). To further verify the LD growth dynamics in HeLa cells under the exposure to a high concentration of FFA, we examined LD growth in live cells over a 2 h period with time-lapse label-free SRS imaging of a fixed field of view (FOV, see Video S2 in the Supporting Information). The statistical analyses of these images confirmed a constant average size and SRS intensity of single LDs during the FFA uptake (Figure 3d), as well as a significant increase in the number of LDs (Figure 3e). All of these single-LD data suggest that the dominant mechanism for storing excessive lipids in HeLa is through increasing the number of LDs.

Single-Lipid-Droplet Distribution in Different Types of Cells. We then asked whether different cell types had unique responses to exogenous FFA. On a single microfluidic device, we cultured four types of cells, HeLa, Chang liver, MCF7, and MDA-MB-231, with titrated OA concentration in each chamber array and two replicated arrays for each cell type (Figure 4),

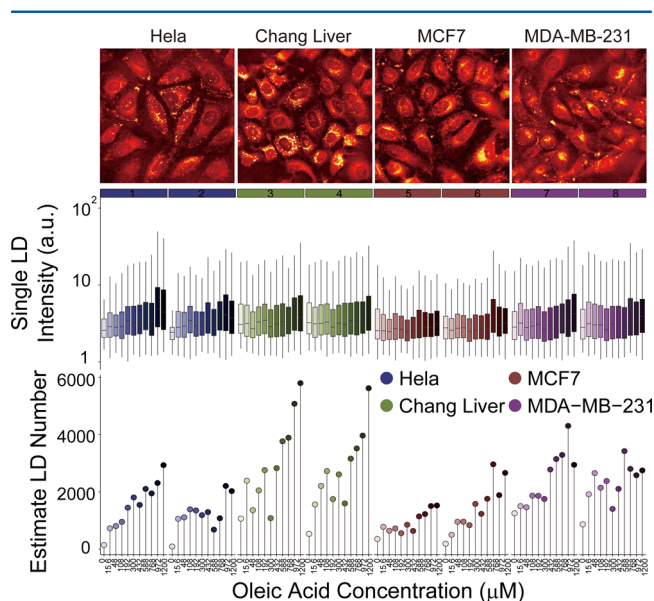


Figure 4. Single-LD distribution among four types of cells (HeLa, Chang Liver, MCF7 and MDA-MB-231). All data shown here was calculated from cells grown on the same chip. The lipid-specific images of four cells were shown in the top panel. The middle panel demonstrates the single-LD intensity distribution, and the bottom panels show the estimated LD numbers.

yielding data from an average of about 500 cells for each type. For all cell types, the SRS intensity (Figure 4) and size (see Figure S9 in the Supporting Information) distribution of single LDs exhibited an insignificant rising trend with an increase of OA concentration. In these cells, the primary mechanism of lipid accumulation is to increase the number of LDs with an increase of extracellular OA (Figure 4), with Chang liver cells displaying the most dramatic variations. This might be attributed to the capacity of lipid uptake of hepatocytes.³²

Lipid Droplet Heterogeneity with Single-Cell Resolution among Different Types of Cells. All the above measurements were performed with single-LD resolution, but we only evaluated the “average” behavior of the cells without

considering cell-to-cell variation. LD heterogeneity between cells has been reported in adipocytes during the process of adipogenesis.³³ For nonadipocyte cells, variability in LD distribution has been mentioned occasionally as an interesting phenomenon but has lacked statistical quantification. Our method provides a general approach to quantitatively characterize the nonadipocytes phenotype on the basis of an accurate assessment of many LDs in single cells. This new measurement may lead to better understanding of the LD regulatory network and the biochemical reaction rate associate with physical parameters of LDs.

To eliminate the sampling bias, we acquired three-dimensional dual-band SRS images of 1174 HeLa cells. For each cell, the total lipid accumulation was estimated by the integrated intensity of all LDs. By quantifying each LD in every single cell, we have shown that, on average, about a 30-fold elevation of total lipid in single cells was observed when extracellular OA increased from 0 to 1.2 mM (P value = 1.216×10^{-4} , Figure 5a). However, a more informative observation was the LD heterogeneity among single cells. Unsupervised clustering shows that at low OA concentration some cells form a large amount of LDs, whereas at high OA concentration, some cells still keep very few LDs (Figure 5b and Figure S10). This dual-band image processing presented cellular heterogeneity more accurately, compared with the FOV sampling (Figure 5c). We hence extended this method to all four cell lines. The population of cells containing more lipid gradually increased with the addition of OA (Figure 5d). We further investigated the number of LDs in every single cell and found a rising trend of more LDs with higher OA concentration (Figure 5e). Notably, the distribution of LD number displayed an analogous pattern with that of total lipid in single cells, supporting our previous observation that the dominant mechanism of LD growth for these cell types is through increased LD number.

Lipid Droplet Distribution in a Single Cells Reflects the Culture Environment. Since single-cell LD heterogeneity is intrinsic, we wondered if it was possible to infer the culture microenvironment of a cell by using the morphological parameters of LDs quantified with our platform. We adopted a rival penalized competitive learning (RPCL)^{34,35} algorithm to classify single cells on the basis of their LD number and total lipid intensity (Figure 6a and Figures S11–S13a in the Supporting Information). In each clustered category, the cells have similar LD characteristics, although they might not be cultured in the same condition. We mapped the cells cultured in different OA concentrations in each cluster and found that the cells with higher total lipid intensity and LD number were more likely to have originated from the high OA culture conditions; furthermore, the cells with lower total lipid and fewer LDs were more likely to have grown in low OA conditions (Figure 6b and Figures S11–S13b). This result confirmed that although there was measurable heterogeneity, increased concentration of the OA treatment was the driving force behind the increased number and intensity of LDs in single cells.

CONCLUSIONS

Morphological changes of cells or cell organelles usually lead to important discoveries in biology. The quantification of phenotype variation is hence of great importance as the precise measurements contribute to the interpretation of underlying biological mechanisms.

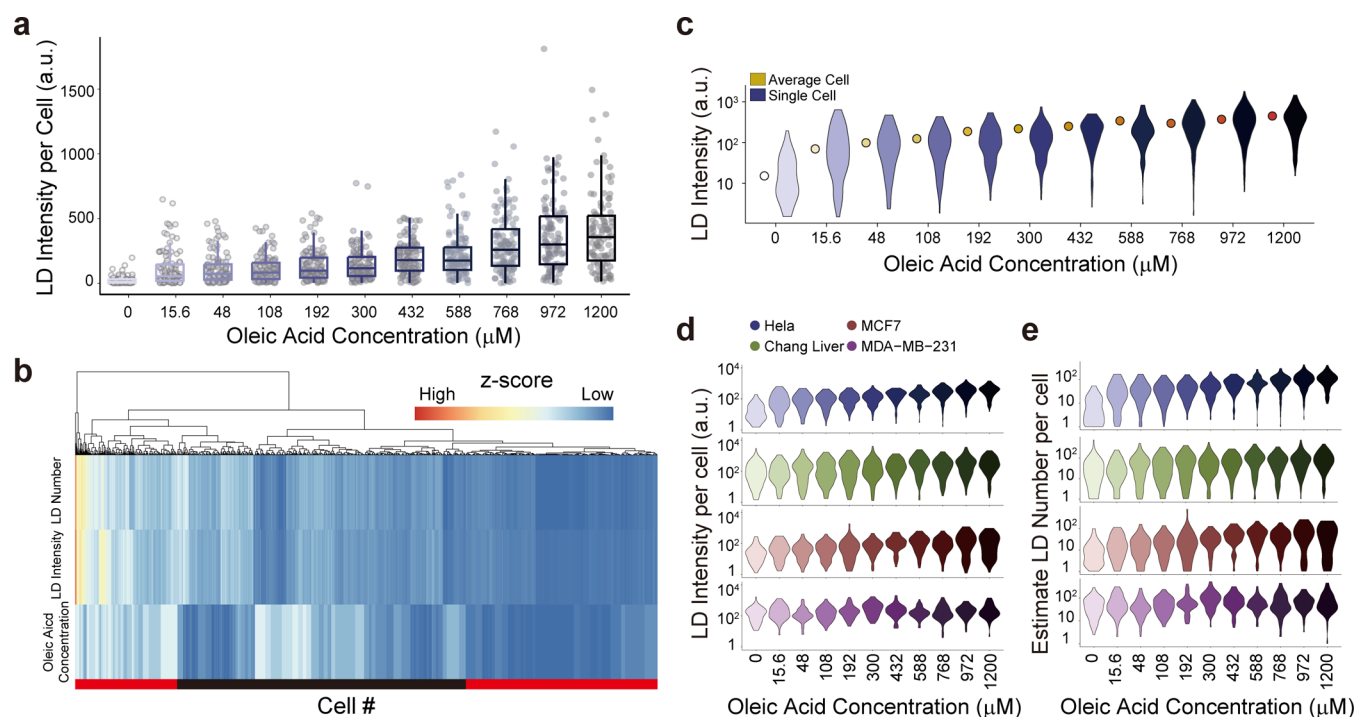


Figure 5. Cell-to-cell variation of LD distribution. (a) The total LD intensity distribution in 1176 HeLa cells under different culture conditions. Each dot denotes the total LD intensity in one cell. (b) Unsupervised hierarchical clustering of HeLa cells based on the LD number, intensity, and the concentration of OA in culture. Each column of the heatmap represents one cell. Though the consistency between LD morphology parameters and the OA concentration existed (red), different patterns of the heatmap show that some cells with high values of LD number and intensity were found to be cultured in low concentration of OA and vice versa (black). (c) The comparison of LD intensity distribution between single HeLa cells and averaged “single” cells. (d,e) The distribution of LD intensity and number in HeLa cells (blue), Chang liver cells (green), MCF7 cells (red), and MDA-MB-231 cells (purple).

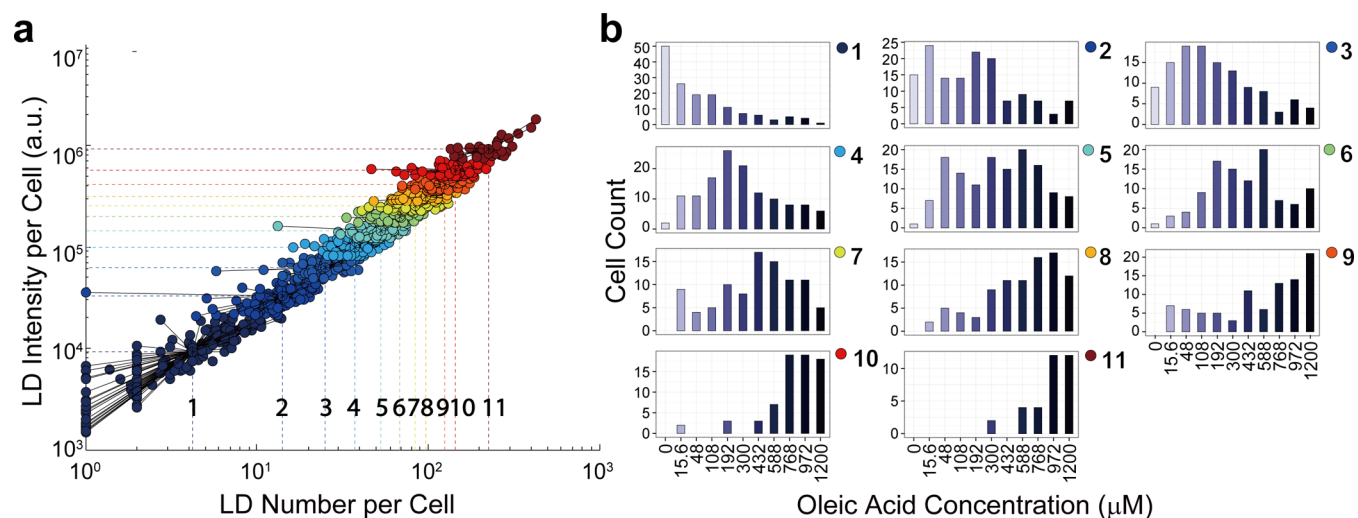


Figure 6. Lipid droplet distribution in single cells reflects the culture environment. (a) Unsupervised RPCL clustering of single HeLa cells. Each dot represents one cell. Clusters are indicated by color, and the intersection of vertical and horizontal lines indicate cluster centers. Clustering tags are shown beneath the cluster centers. (b) In each cluster, cells cultured in each concentration of OA were counted and plotted to illustrate the dominant groups of the original culture environment.

In this report, we coupled a microfluidic device with stimulated Raman scattering microscopy for the in situ analysis of lipid droplet morphology in live cells. The microfluidic platform enables high-throughput cell culture under varying conditions; multiple cell type handling; automated, parallel, and precise delivery of chemicals; and smaller demand for cell number. Additionally, nonlinear optical imaging offers advantages for chemical characterization of single cells.³⁶ The

detection specificity of lipid droplet by SRS microscopy is high,³⁷ and the label-free feature of SRS microscopy allows long-term observation of live cells under nearly physiological conditions. The spatial resolution of SRS microscopy is diffraction limited and comparable with other light microscopy. Compared with fluorescent labeling, the characteristics of SRS microscopy makes the quantification of lipid more precise and straightforward as the intensity of SRS signal is proportional to

the number of chemical bonds in the detection foci. To avoid obscuring the variable response from individual cells by averaged measurement of a large population, lipid droplet analysis with single-cell resolution is achieved by dual-channel imaging and automated image processing. We applied this platform to investigate lipid uptake when cells were under the stimulation of different concentrations of oleic acid.

The combination of SRS microscopy with microfluidic technology offers the capability of precise quantification of cell phenotypes which are represented in lipid droplet morphology. This platform will be powerful when applied to lipid-metabolism-related culture-condition optimization and drug-response screening, as it enables the measurements of multiple cell types' response to multiple stimuli with complex temporal inputs at the single-cell level. Moreover, the phenotype screening system described here is ideally suited to combine with genotype analysis tools for more thorough investigation. For example, some microfluidic devices have been reported to be applied in the whole-transcriptome sequencing.^{38,39} The incorporation of the phenotype characterizing and the sequencing microfluidic chip and imaging can, in theory, achieve in situ cell clone selection and sequencing with less external interference and human operation bias. This improvement has great importance for untangling basic molecular evidence and accelerating progress in medicine and biotechnology.

■ ASSOCIATED CONTENT

● Supporting Information

The Supporting Information is available free of charge on the ACS Publications website at DOI: [10.1021/acs.analchem.6b00862](https://doi.org/10.1021/acs.analchem.6b00862).

Experimental details including microfluidic chip fabrication, cell culture in dishes, mixing efficiency evaluation, stimulated Raman scattering microscopy, statistical analysis, and Figures S1–S13 (PDF)

Video S1: Mixing with valves; video S2: Time-lapse label-free SRS imaging (ZIP)

■ AUTHOR INFORMATION

Corresponding Authors

*E-mail: astreet@berkeley.edu (A.M.S.).

*E-mail: yanyi@pku.edu.cn (Y.H.).

Present Address

§(A.M.S.) Department of Bioengineering, University of California, Berkeley, Berkeley, California 94709, United States.

Author Contributions

A.M.S and Y.H conceived the project. A.M.S and C.C. designed the microfluidic chip. C.C. performed the chip fabrication and cell culture experiment. C.C and T.C. performed SRS imaging. D.Z., T.C., and C.C. developed the lipid droplet quantification algorithm. D.Z. and C.C. wrote the software. C.C. performed the statistical analysis. C.C. and Y.H wrote the manuscript.

Notes

The authors declare no competing financial interest.

■ ACKNOWLEDGMENTS

We thank Wenli Zheng for RPCL clustering suggestion and help. This work was supported by the National Natural Science Foundation of China (Grant 21327808 and 21525521).

■ REFERENCES

- (1) Varlamov, O.; Somwar, R.; Cornea, A.; Kievit, P.; Grove, K. L.; Roberts, C. T. *Am. J. Physiol-Endoc. M.* **2010**, *299*, E486–E496.
- (2) Raj, A.; Peskin, C. S.; Tranchina, D.; Vargas, D. Y.; Tyagi, S. *PLoS Biol.* **2006**, *4*, e309.
- (3) Herms, A.; Bosch, M.; Ariotti, N.; Reddy, B. J.; Fajardo, A.; Fernandez-Vidal, A.; Alvarez-Guaita, A.; Fernandez-Rojo, M. A.; Rentero, C.; Tebar, F.; Enrich, C.; Geli, M. I.; Parton, R. G.; Gross, S. P.; Pol, A. *Curr. Biol.* **2013**, *23*, 1489–1496.
- (4) Walther, T. C.; Farese, R. V., Jr. *Annu. Rev. Biochem.* **2012**, *81*, 687–714.
- (5) Varlamov, O.; Somwar, R.; Cornea, A.; Kievit, P.; Grove, K. L.; Roberts, C. T., Jr. *Am. J. Physiol-Endoc. M.* **2010**, *299*, E486–E496.
- (6) Rosen, E. D.; Spiegelman, B. M. *Nature* **2006**, *444*, 847–853.
- (7) Suzuki, M.; Shinohara, Y.; Ohsaki, Y.; Fujimoto, T. *Microscopy* **2011**, *60*, S101–116.
- (8) Thiam, A. R.; Farese, R. V., Jr.; Walther, T. C. *Nat. Rev. Mol. Cell Biol.* **2013**, *14*, 775–786.
- (9) Le, T. T.; Cheng, J. X. *PLoS One* **2009**, *4*, e5189.
- (10) Chumnannpuen, P.; Brackmann, C.; Nandy, S. K.; Chatzipapadopoulos, S.; Nielsen, J.; Enejder, A. *Biotechnol. J.* **2012**, *7*, 594–601.
- (11) Rosen, E. D.; MacDougald, O. A. *Nat. Rev. Mol. Cell Biol.* **2006**, *7*, 885–896.
- (12) Gomez-Sjoberg, R.; Leyrat, A. A.; Pirone, D. M.; Chen, C. S.; Quake, S. R. *Anal. Chem.* **2007**, *79*, 8557–8563.
- (13) Tay, S.; Hughey, J. J.; Lee, T. K.; Lipniacki, T.; Quake, S. R.; Covert, M. W. *Nature* **2010**, *466*, 267–271.
- (14) Lecault, V.; Vaninsberghe, M.; Sekulovic, S.; Knapp, D. J.; Wohrer, S.; Bowden, W.; Viel, F.; McLaughlin, T.; Jarandehi, A.; Miller, M.; Falconnet, D.; White, A. K.; Kent, D. G.; Copley, M. R.; Taghipour, F.; Eaves, C. J.; Humphries, R. K.; Piret, J. M.; Hansen, C. L. *Nat. Methods* **2011**, *8*, 581–586.
- (15) Boneschansker, L.; Yan, J.; Wong, E.; Briscoe, D. M.; Irimia, D. *Nat. Commun.* **2014**, *5*, 4787.
- (16) Hansen, A. S.; Hao, N.; O'Shea, E. K. *Nat. Protoc.* **2015**, *10*, 1181–1197.
- (17) Kellogg, R. A.; Gomez-Sjoberg, R.; Leyrat, A. A.; Tay, S. *Nat. Protoc.* **2014**, *9*, 1713–1726.
- (18) Ng, A. H.; Dean Chamberlain, M.; Situ, H.; Lee, V.; Wheeler, A. R. *Nat. Commun.* **2015**, *6*, 7513.
- (19) Novak, R.; Hart, K.; Mathies, R. A. *Nucleic Acids Res.* **2015**, *43*, e104.
- (20) Sarkar, A.; Kolitz, S.; Lauffenburger, D. A.; Han, J. *Nat. Commun.* **2014**, *5*, 3421.
- (21) Baumgart, T.; Hammond, A. T.; Sengupta, P.; Hess, S. T.; Holowka, D. A.; Baird, B. A.; Webb, W. W. *Proc. Natl. Acad. Sci. U. S. A.* **2007**, *104*, 3165–3170.
- (22) Kuerschner, L.; Ejsing, C. S.; Ekroos, K.; Shevchenko, A.; Anderson, K. I.; Thiele, C. *Nat. Methods* **2005**, *2*, 39–45.
- (23) Listenberger, L. L.; Brown, D. A. *Current Protocols in Cell Biology*; John Wiley & Sons, Inc.: Hoboken, NJ, 2001.
- (24) O'Rourke, E. J.; Soukas, A. A.; Carr, C. E.; Ruvkun, G. *Cell Metab.* **2009**, *10*, 430–435.
- (25) Le, T. T.; Yue, S.; Cheng, J. X. *J. Lipid Res.* **2010**, *51*, 3091–3102.
- (26) Freudiger, C. W.; Min, W.; Saar, B. G.; Lu, S.; Holtom, G. R.; He, C. W.; Tsai, J. C.; Kang, J. X.; Xie, X. S. *Science* **2008**, *322*, 1857–1861.
- (27) Wang, P.; Li, J. J.; Wang, P.; Hu, C. R.; Zhang, D. L.; Sturek, M.; Cheng, J. X. *Angew. Chem., Int. Ed.* **2013**, *52*, 13042–13046.
- (28) Wang, P.; Liu, B.; Zhang, D. L.; Belew, M. Y.; Tissenbaum, H. A.; Cheng, J. X. *Angew. Chem., Int. Ed.* **2014**, *53*, 11787–11792.
- (29) Yue, S. H.; Li, J. J.; Lee, S. Y.; Lee, H. J.; Shao, T.; Song, B.; Cheng, L.; Masterson, T. A.; Liu, X. Q.; Ratliff, T. L.; Cheng, J. X. *Cell Metab.* **2014**, *19*, 393–406.
- (30) Fu, D.; Yu, Y.; Follick, A.; Currie, E.; Farese, R. V.; Tsai, T. H.; Xie, X. S.; Wang, M. C. *J. Am. Chem. Soc.* **2014**, *136*, 8820–8828.
- (31) Otsu, N. *IEEE Trans. Syst. T. Man. Cyb.* **1979**, *9*, 62–66.

- (32) Bradbury, M. W. *Am. J. Physiol. Gastr. L.* **2006**, *290*, G194–G198.
- (33) Loo, L. H.; Lin, H. J.; Singh, D. K.; Lyons, K. M.; Altschuler, S. J.; Wu, L. F. *J. Cell Biol.* **2009**, *187*, 375–384.
- (34) Ma, J. W.; Wang, T. J. *IEEE Trans. Syst. Man. Cybern. B Cybern.* **2006**, *36*, 722–737.
- (35) Ma, J. W.; Cao, B. *Lect. Notes Comput. Sc.* **2006**, *3971*, 442–447.
- (36) Streets, A. M.; Li, A.; Chen, T.; Huang, Y. *Anal. Chem.* **2014**, *86*, 8506–8513.
- (37) Wang, M. C.; Min, W.; Freudiger, C. W.; Ruvkun, G.; Xie, X. S. *Nat. Methods* **2011**, *8*, 135–138.
- (38) Wu, A. R.; Neff, N. F.; Kalisky, T.; Dalerba, P.; Treutlein, B.; Rothenberg, M. E.; Mburu, F. M.; Mantalas, G. L.; Sim, S.; Clarke, M. F.; Quake, S. R. *Nat. Methods* **2013**, *11*, 41–46.
- (39) Streets, A. M.; Zhang, X.; Cao, C.; Pang, Y.; Wu, X.; Xiong, L.; Yang, L.; Fu, Y.; Zhao, L.; Tang, F.; Huang, Y. *Proc. Natl. Acad. Sci. U. S. A.* **2014**, *111*, 7048–7053.